

1 Neutron-Neutron Correlations in the Photofission of U-238

2 J. Burggraf, D.S. Dale, and T. Forest
3

4 *Department of Physics,*
5 *Idaho State University, Pocatello, ID 83201*

6 G. Warren, S. Stave, S. Behling, and E. Church
7

8 *Pacific Northwest National Laboratory, PO Box 999, Richland, Washington 99352*

(Dated: March 11, 2019)

9 **Background:** In the fission of actinides, the nearly back-to-back motion of the fission fragments has a strong
10 effect on the kinematics of fission neutrons. This leads to a favoring of opening angles near 0° and 180° in the
11 neutron-neutron (n-n) opening angle distributions of correlated neutron pairs from the same fission event.

12 **Purpose:** To measure the n-n opening angle and energy correlations in the photofission of ^{238}U . As of this
13 writing, measurements of correlated n-n opening angle distributions have been reported only for the spontaneous
14 and neutron-induced fission of actinides. This work is the first to report such a measurement using photofission
15 and will provide useful experimental input for photofission models used in codes such as MCNP and FREYA.

16 **Method:** Fission is induced using bremsstrahlung photons produced via a low duty factor, pulsed, linear electron
17 accelerator. The bremsstrahlung photon beam impinges upon a ^{238}U target that is surrounded by a large neutron
18 scintillation detection system capable of measuring particle position and time of flight, from which n-n opening
19 angle and energy are measured. Neutron-neutron angular correlations are determined by taking the ratio between
20 a correlated neutron distribution and an uncorrelated neutron distribution formed by the pairing of neutrons pro-
21 duced during different beam pulses. This analysis technique greatly diminishes effects due to detector efficiencies,
22 acceptance, and experimental drifts.

23 **Results:** The angular correlation of neutrons from the photofission of ^{238}U shows a high dependence on neutron
24 energy as well as a dependence on the angle of the emitted neutrons with respect to the incoming photon beam.
25 Angular correlations were also measured using neutrons from the spontaneous fission of ^{252}Cf , showing good
26 agreement with past measurements.

27 **Conclusions:** The measured angular correlations reflect the underlying back-to-back nature of the fission frag-
28 ments. An anomalous decline in n-n yield was observed for opening angles near 180° .

29 CONTENTS

I. Introduction	50	A. Correlated <i>versus</i> uncorrelated n-n energy distribution	11
A. Fission and Neutron Correlations	51	B. Detector Cross-talk	11
B. Past Measurements of Spontaneous and	52	1. Simulation of Detector Cross-talk	12
Neutron Induced Fission	53	C. Neutron Scattering within Target	13
II. Experimental Setup	54	VI. Results	14
A. Detectors	55	A. n-n angular correlation <i>versus</i> neutron energy	14
B. Detector Shielding	56	B. Considering θ_{abs}	15
C. Bremsstrahlung Photon Beam	57	VII. Concluding Remarks	17
D. DU Target	58	VIII. Acknowledgments	17
E. Electronics	59	References	17
III. Measurement Techniques	60	I. INTRODUCTION	17
A. Particle Time of Flight and Energy Determination	61	A. Fission and Neutron Correlations	17
B. Particle Position Reconstruction	62	The photofission reaction occurs during the de- 64 excitation of a nucleus after the absorption of a pho- 65 ton. For photon energies between 6 and 25 MeV, this ab- 66 sorption occurs primarily via the giant dipole resonance 67 (GDR). One distinct and useful aspect of photofission, 68	17
C. Measurements with ^{252}Cf	63		
IV. Analysis	64		
A. Cancelation of Detector Efficiencies, Drifts, and Geometric Phase Space	65		
B. Subtraction of Accidental Coincidences	66		
V. Potential sources of error	67		

particularly when compared to neutron-induced fission, is the simple set of selection rules for the transfer of angular momentum. In photofission, there is a relatively low transfer of angular momentum to the nucleus. For the photofission of even-even nuclei, excitation occurs primarily via electric dipole transitions, and to a lesser extent electric quadrupole transitions, which gives rise to anisotropies in the fission fragment angular distribution that are far more pronounced than for other types of fission [1]. Because of this angular momentum selectivity, photofission is commonly used as a means to study sub-nuclear structures and the fundamentals of the fission process. As such, detailed studies of fission are needed in order to dial in various model parameters required for an accurate theoretical description of fission.

Neutron emission in fission can be classified into two categories depending on the time of emission: delayed and prompt. Prompt fission neutrons are defined as neutrons that are emitted either immediately after ($< 10^{-14}$ seconds) fission, or, during the scission of the nucleus, and account for $\sim 99\%$ of neutron emission [2]. Delayed neutrons account for only $\sim 1\%$ of total neutron emission in actinide photofission [2], and, emitted milliseconds to minutes after fission, are not relevant here because this measurement is insensitive to them.

Prompt fission neutron production occurs by means of two distinct mechanisms. The dominant mechanism is neutron emission from the fully accelerated fragments. The second mechanism, referred to as *early* or *scission* neutron emission, is the emission of neutrons during either the scission of the nucleus or the acceleration of the fission fragments. A large number of past studies have established that the majority of prompt fission neutrons (80%–98%) are emitted from the fully accelerated fragments, while scission neutrons account for the remaining 2%–20% percent [3]. The nature of scission neutrons has remained elusive since their first tentative observation in 1962 by Bowman *et al.* [4].

A useful observational input for prompt neutron modeling is the neutron-neutron (n-n) opening angle distribution of correlated neutron pairs, as seen in the lab frame, hereafter denoted θ_{nn} . There are, on average, about 2 or 3 neutrons released per fission, depending on the target isotope and how the fission is induced. It has been shown that neutrons released from the fully accelerated fission fragments are evaporated isotropically in the fragment's rest frame, and are emitted at speeds comparable to that of the fragments themselves [5]. This leads to the well-known U-shaped distribution in θ_{nn} , which has been reported in studies of neutron-induced, spontaneous, and, in this study, photon-induced fission. An example of such distribution is seen in Fig. 1.

The U-shaped distribution of θ_{nn} can be understood as the result of the boost provided to the neutrons by the fission fragments in binary fission. Due to the conservation of momentum, the fully accelerated fission fragments are traveling nearly back-to-back, and neutrons emitted from different fragments are boosted in opposite direc-

tions, whereas neutrons emitted from the same fragment are boosted in the same direction. Thus, because the velocities of the fission fragments are large enough to account for a significant portion of the kinetic energy of fission neutrons, neutron pairs emitted from the accelerated fragments exhibit a favoring of opening angles near 0° if emitted from the same fragment and 180° if emitted from different fragments, and, consequently, a suppression of opening angles near 90° .

The favoring of large and small n-n opening angles shows a strong dependence on neutron energy. Neutrons with higher energy are more likely to have been emitted along the same direction as the fission fragments and are therefore expected to favor large and small opening angles. The θ_{nn} distribution and its dependence on neutron energy are expected to shed light on several fundamental aspects of the fission process including the neutron multiplicity distributions associated with the light and heavy fission fragments, the nuclear temperatures of the fission fragments, and the mass distribution of the fission fragments as a function of energy released. In addition, the unique kinematics of fission and the resulting n-n correlations have the potential to be the basis for a new tool to characterize fissionable materials [6].

B. Past Measurements of Spontaneous and Neutron Induced Fission

As of this writing, tabulated data for photofission is far scarcer than for neutron induced fission. The first measurement of the angular correlation among coincident neutrons from fission was performed by Debenedetti *et al.* [7] in 1948 from neutron induced fission of ^{235}U . The next measurement of this type was performed by Pringle and Brooks in 1975 [8], in which neutrons emitted from the spontaneous fission (SF) of ^{252}Cf were found to have high coincidence rates at small opening angles near 0° and large opening angles near 180° . In order to produce a result that is insensitive to the effects of detector geometry and efficiency, the present work uses techniques similar to those used in reference [8], in which a ratio is taken between a correlated opening angle distribution and an uncorrelated opening angle distribution.

To date, numerous measurements of n-n angular correlation using ^{252}Cf have been performed [8–11]. This makes ^{252}Cf a good benchmark for n-n angular correlation measurements. Fig. 1 compares measurements in this work to past measurements of n-n correlations in the SF of ^{252}Cf . Correlated n-n measurements have also been performed using thermal induced fission of ^{235}U , ^{233}U , and ^{239}Pu [12].

II. EXPERIMENTAL SETUP

This experiment was carried out at the Idaho Accelerator Center (IAC), using their short-pulsed linear acceler-

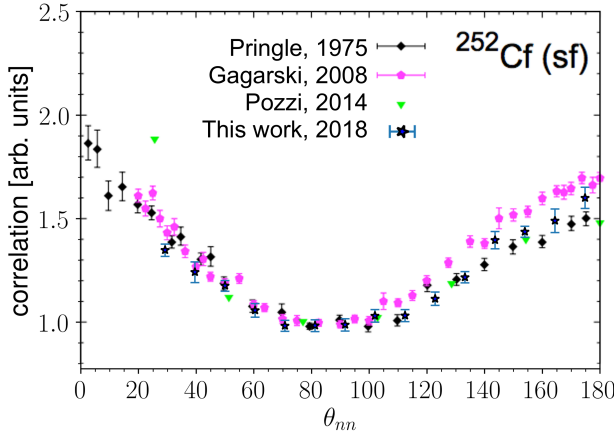


FIG. 1: θ_{nn} distribution from the spontaneous fission of ^{252}Cf . The neutron detection threshold for Pringle [8], Gagarski [11], and Pozzi [13] is 0.425 MeV, 0.425 MeV, and 0.7 MeV, respectively, and for this work is 0.5 MeV.

ator, which is an L-band frequency (1300 MHz) electron linear accelerator. See section II C for the accelerator parameters used during the experiment. Figure 2 shows a top-down diagram of the experimental arrangement.

The detection system measures neutron position and time of flight (ToF), which is defined as the time taken for a particle to travel from the fission target to a detector. The purpose of the ToF measurement is to determine the kinetic energy of detected neutrons and to distinguish between photons and neutrons. The detection system's positional precision is ± 9 cm, which gives an average angular precision of $\pm 6^\circ$ in opening angle reconstruction.

The detection system consists of fourteen shielded scintillators made from Polyvinyl Toluene (PVT) arranged in a ring around the target (see Figs. 2 and 3). Attached to both ends of each scintillator are 10-cm long, non-scintillating, ultra-violet transmitting, plastic light-guides. A Hamamatsu 580-17 photomultiplier (PMT) tube is fixed to each light-guide using optical glue. In order to increase the chance that scintillation light remains inside the scintillator, the scintillators were polished to remove micro-imperfections and were then wrapped in reflective aluminized mylar.

Ten out of the fourteen scintillators had dimensions of $76.2 \times 15.2 \times 3.8$ cm 3 . The remaining four, the forward-most detectors located at $\pm 30^\circ$ with respect to the beam, had dimensions of $25.4 \times 15.2 \times 3.8$ cm 3 . These scintillators, $1/3$ the length of the rest, are the result of the segmentation of two normally sized scintillators in order to address the high photon flux at these locations caused by the forward scattering of photons from the target. Prior to segmentation, a photon was registered in the forward-most detectors at a rate of about 0.9 photons per

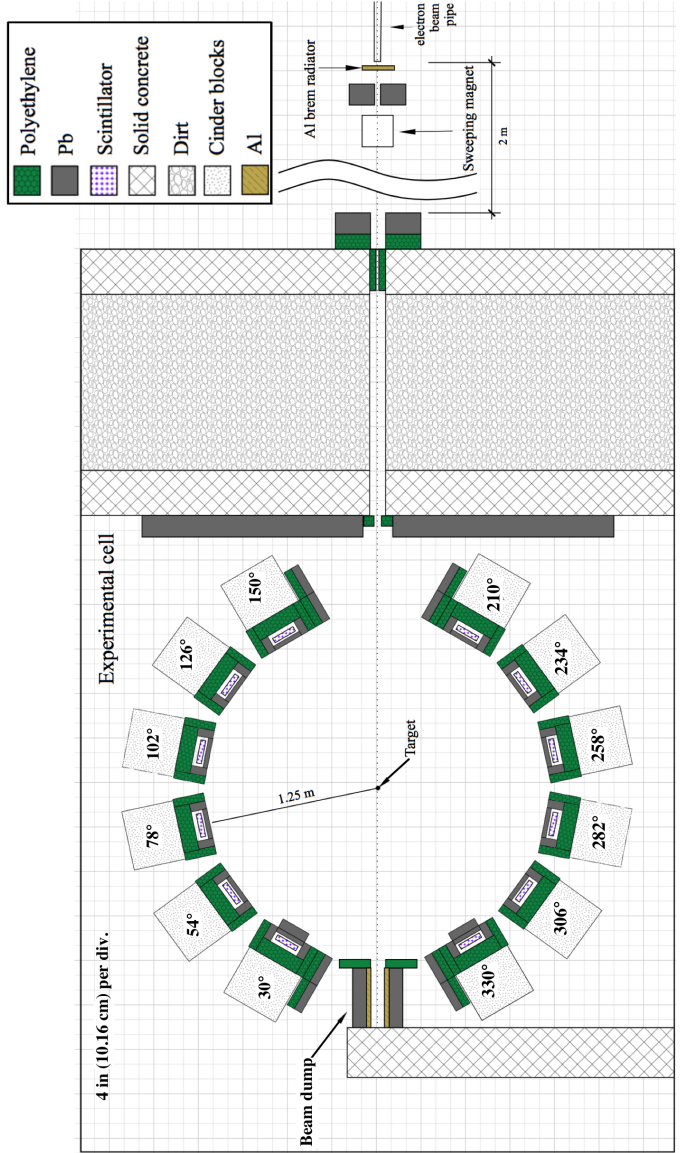


FIG. 2: To-scale, top down diagram of the experimental setup. An electron beam impinges upon a 3.8 cm thick Al radiator, and the resulting bremsstrahlung beam enters the experimental cell from the top. The supporting structure for each detector has been labeled according to the angle, in degrees, between the center of each detector and direction of the incoming photon beam.

pulse, and because the electronics were operated in single hit mode, this greatly reduced the effective neutron detection efficiency. After segmentation and optimization of shielding, the photon detection rate was about 0.2 photons per pulse in each segmented detector. The segmented detectors also differ from the rest in that they were instrumented with only a single PMT, and therefore provide a comparatively lower precision in energy and position measurements. In order to test for systematic errors that may have resulted from the use of the segmented detectors, opening angle measurements were

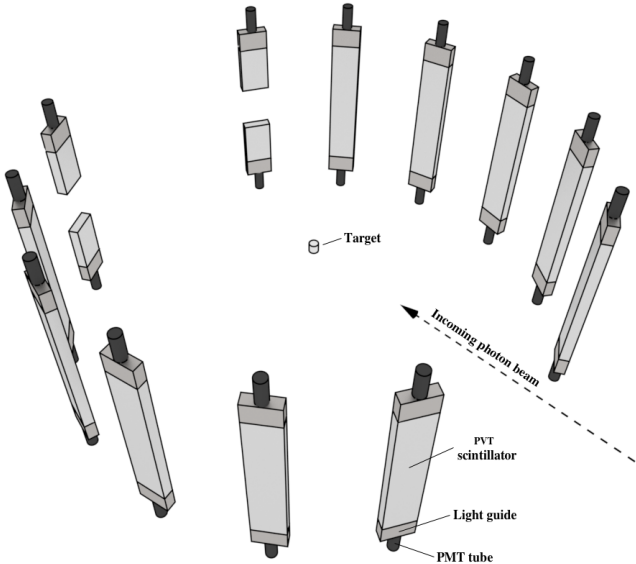


FIG. 3: 3-D render of the bare, unshielded scintillators, along with PMTs and light guides.

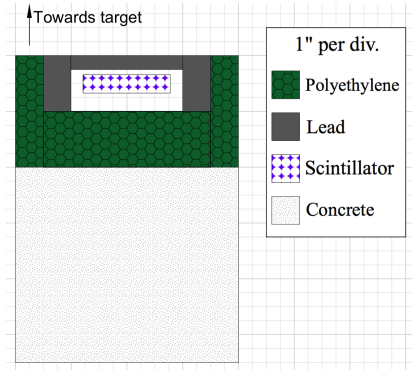


FIG. 5: Detector shielding was designed to reduce the detection of photons, room return, and detector cross-talk.

236

B. Detector Shielding

237 The detector shielding, depicted in Fig. 5, was con-
238 structed using lead and polyethylene with the aim of re-
239 ducing detector cross-talk, the detection of photons, and
240 noise. The sides of each scintillator were shielded with
241 5 cm of lead followed by 5 cm of polyethylene to reduce
242 the chance of neutron cross-talk. Lead was not placed
243 behind the scintillators after an MCNP-POLIMI simula-
244 tion indicated it would occur at significant rates other-
245 wise. Instead, 10 cm of polyethylene was placed behind
246 the scintillators. For a detailed discussion about the issue
247 of cross-talk, see section V B.

248 The front face of each detector was subject to
249 the highest photon flux due to the scattering of the
250 bremsstrahlung beam from the target. The detection of
251 a photon renders the given detector unable to detect any
252 subsequent fission neutrons from the same pulse due to
253 the detector recovery time. Lead mitigates this prob-
254 lem by reducing photon flux, but has the side effect of
255 scattering neutrons. If a neutron scatters prior to being
256 detected, the ToF measurement and position reconstruc-
257 tion are incorrect. The extent of measurement errors
258 caused by lead shielding were quantified using an MCNP
259 simulation, and, accordingly, 2.5 cm of lead was placed
260 along the front face of the detectors. This diminished
261 photon detection rates to reasonable levels, and, accord-
262 ing to the simulation, leads to a root-mean-square error
263 in opening angle and ToF of 1° and 0.3 ns, respectively,
264 due to neutron elastic scattering.

265 Because of the particularly high photon flux at the
266 sides of all detectors located directly adjacent to the
267 beam, an additional 2" of lead was placed along the sides
268 of these detectors. For the same reason, an additional 2"
269 of lead was also placed along the front faces of the de-
270 tectors farthest downstream, located at ±30° from the
271 beam line. The differences in shielding design among the
272 detectors can be seen in Fig. 2.

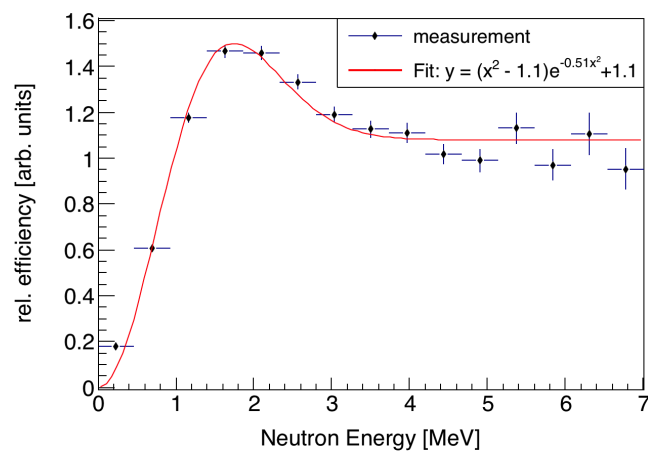


FIG. 4: The overall relative efficiency of the neutron detection system as a function of neutron energy is calculated by dividing the measured energy distribution by the theoretical energy distribution of neutrons from the SF of ^{252}Cf .

226 compared with and without their use, and the differences
227 were well within experimental errors.

228 The relative efficiencies of the neutron detectors as a
229 function of neutron energy were calculated by dividing
230 measured and known yields from the SF of ^{252}Cf taken
231 from MCNP. The results are shown in Fig. 4, which is
232 produced from the aggregate of events in all detectors.
233 See section IV for a discussion of how the effects of de-
234 tector efficiency are accounted for in this work.

274

C. Bremsstrahlung Photon Beam

In order to ensure that all correlated neutrons produced are due to fission, the bremsstrahlung end-point was set to 10.5 MeV, safely below the $(\gamma, 2n)$ threshold of 11.28 MeV for ^{238}U . Aluminum was chosen for the bremsstrahlung radiator because it has a neutron knock-out threshold above the energy of the electron beam, which ensured that the radiator would not be a source of fast neutrons with the potential to interfere with the experiment. Downstream from the bremsstrahlung radiator is a sweeping magnet that removes charged particles from the photon beam. Next, the beam traveled through a series of polyethylene and lead collimators on its way into the experimental cell in which the target was located (see Fig. 2). Figure 6 shows the energy distribution of photons that reach the target according to an MCNP simulation that modeled the collimation and production of the bremsstrahlung photons.

The electron beam pulse width was set to 3 ns at a repetition rate of 240 Hz with a 1.1 A peak current. The 3 ns pulse width was small compared to the median neutron ToF of 80 ns, and thus made a small contribution to the uncertainty in the neutron energy determination.

297

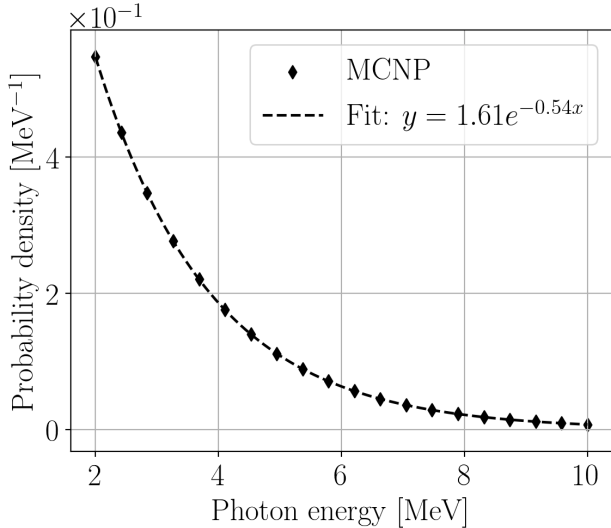


FIG. 6: MCNP simulation of the energy distribution of the bremsstrahlung photons that reach the fission target. Photons with an energy below 2 MeV are excluded.

298

299

300

D. DU Target

A depleted uranium (DU) target in the shape of a thin strip with dimensions of $4 \times 2 \times 0.05 \text{ cm}^3$ was used as the primary target. ^{238}U was chosen as the fission target because it is an even-even nucleus, and as a consequence, the fission fragments are emitted with a high degree of anisotropy with respect to the photon beam direction [1].

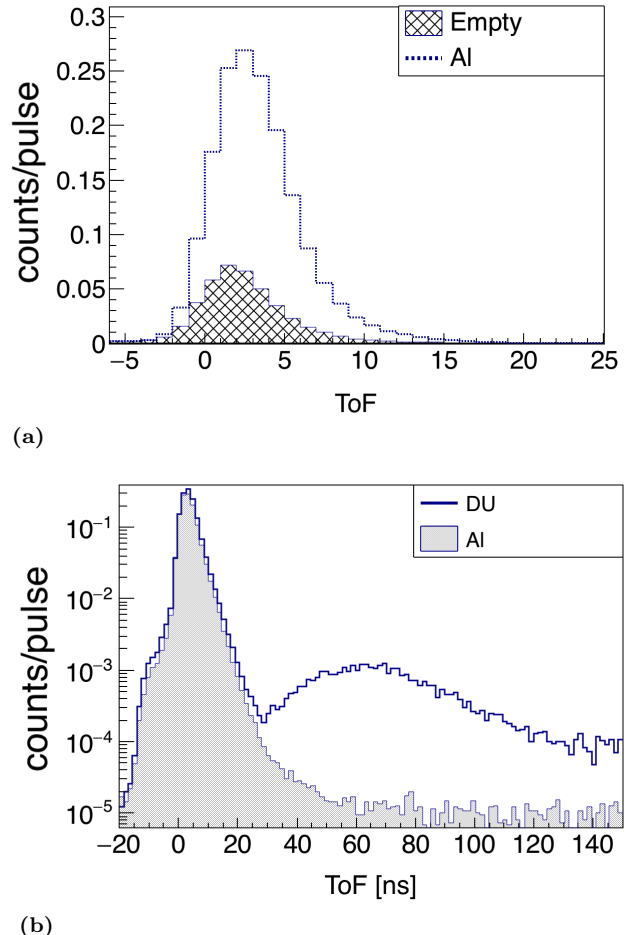


FIG. 7: (a) Comparison between the ToF spectrum of a non-neutron producing target made from Al, to the ToF spectrum produced when no target is used. The large increase in events around 4 ns is due to photons that scatter from the Al target. When no target is in place, sources of the peak seen here is used to find the timing offsets that make it so $t = 0$ corresponds to the moment of fission. (b) Comparison between the Al and DU targets show a pronounced increase in events between 35 and 130 ns due to the introduction of neutrons.

Any target comprised of heavy nuclei has a significant potential to scatter fission neutrons before they exit the target, which is a cause for concern, because neutrons that scatter from heavy nuclei are likely to be deflected at large angles, resulting in the measurement of θ_{nn} 's unconnected to the underlying fission kinematics. The rate of θ_{nn} 's perturbed by neutron scattering within the ^{238}U target was estimated by an MCNP simulation to be 6%. Moreover, it is more likely that neutrons emitted along the wide, 2 cm, axis of the ^{238}U target undergo a scattering event than neutrons emitted along the thinnest, 0.05 cm, axis. As a result, detectors located collinear to the widest axis of the target would see relatively fewer neutrons due to increased scattering along this axis. This bias is removed by slowly rotating the target about the

322 vertical axis during data acquisition at a rate of one rotation per 8 seconds. See section V C for discussion of issues
 323 regarding neutron scattering within the fission target.
 324

325 **E. Electronics**

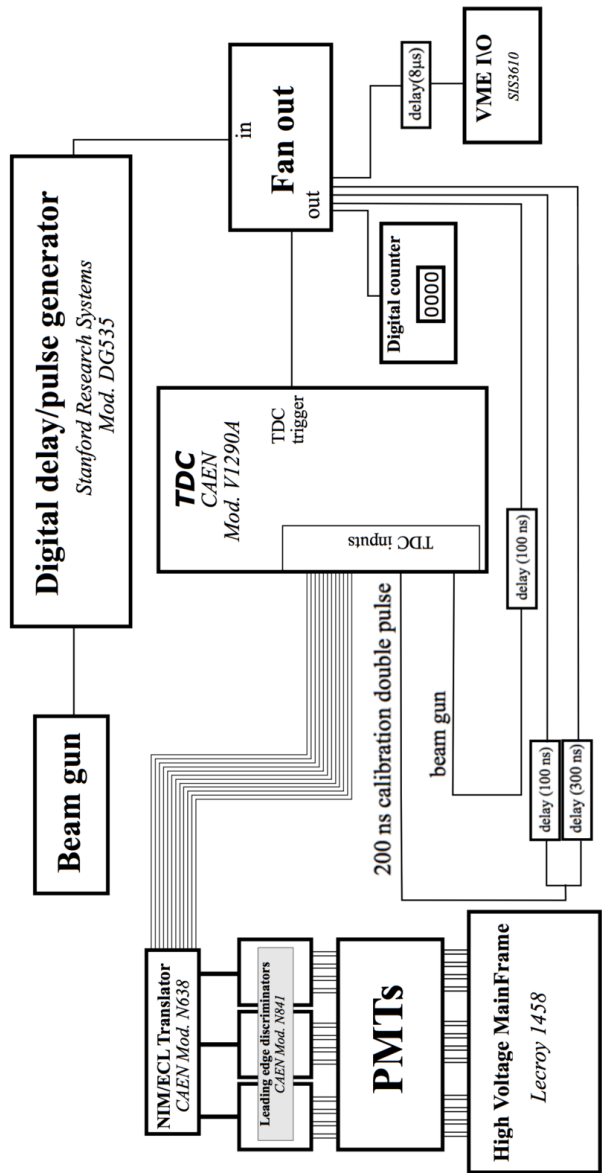
326 A data acquisition system based on NIM/VME standards was used. A schematic of the data acquisition logic
 327 is shown in Figure 8. The PMTs are supplied negative
 328 voltages ranging from 1300 to 1500 V by a LeCroy 1458
 329 high voltage mainframe. Analog signals from the PMTs
 330 were fed into a leading edge discriminator (CAEN Mod.
 331 N841) with input thresholds ranging from 30 mV to 50
 332 mV. The threshold and supply voltages were determined
 333 on a case by case basis for each detector so as to mini-
 334 mize noise, while also matching the efficiencies of all the
 335 detectors as closely as possible. Logic signals from the
 336 discriminator were converted to ECL logic and fed into a
 337 CAEN model V1290A TDC. The timing of signals from
 338 the PMTs were always measured relative to a signal from
 339 the accelerator provided at the beginning of each pulse.
 340 Even though a multi-hit TDC was being used, only the
 341 first signal from any given PMT is used each pulse due to
 342 concerns over dead-time within the electronics and sig-
 343 nal reflections within the cables. On the software side,
 344 the CODA [14] software package developed by Jefferson
 345 Laboratory was used to read out the data from the TDC
 346 and digitally store it for analysis.
 347

348 III. MEASUREMENT TECHNIQUES

349 A. Particle Time of Flight and Energy 350 Determination

351 The ToF of detected particles is used to distinguish
 352 between neutrons and photons and to determine neutron
 353 energy. A particle's reconstructed position is used to de-
 354 termine direction of motion, which is then used to calcu-
 355 late the opening angle between pairs of detected particles.
 356 Position and ToF are each determined using the timing
 357 of coincident signals from both PMTs of a detector.

358 The sum of the times required for scintillation light
 359 to travel from the point of scintillation to both PMTs
 360 is equal to the time required for the light to travel the
 361 full length of the scintillator, which is a constant for light
 362 that travels parallel to the length of the scintillator. This
 363 is supported by data, shown in Fig. 9, which were pro-
 364 duced from a series of tests in which a collimated ^{60}Co
 365 source was placed at seven different locations along a
 366 scintillator. One of the two coincident photons emitted
 367 by ^{60}Co reaches the scintillator and the other is detected
 368 by an auxiliary detector serving as the trigger. The pho-
 369 tons incident on the scintillator have a spot size of less
 370 than 1 cm due to source collimation. These events all
 371 have equal transit time, regardless of the ^{60}Co source's
 372 position.



373 **FIG. 8:** Wiring diagram of the electronics setup.
 374

375 In Fig. 9(a), it can be seen that the time required for
 376 the scintillation light to propagate through the scintilla-
 377 tor has a large effect on the timing of each PMT alone,
 378 however, the average of the times of both PMTs is a con-
 379 stant, unaffected by the location at which the particle
 380 undergoes scintillation. For this reason, taking the aver-
 381 age of signals from two PMTs is advantageous because it
 382 removes the roughly 5 ns timing error that would other-
 383 wise exist due to the time required for scintillation light
 384 to propagate through the scintillator. The requirement
 385 that there be coincident events in both of a detector's
 386 PMTs also aids in reducing noise.

387 During photofission measurements, ToF is calculated
 388 by the following expression:

$$\text{ToF} = t_{\text{avg}}^{\text{PMT}s} - t_{\text{beam}} + C, \quad (1)$$

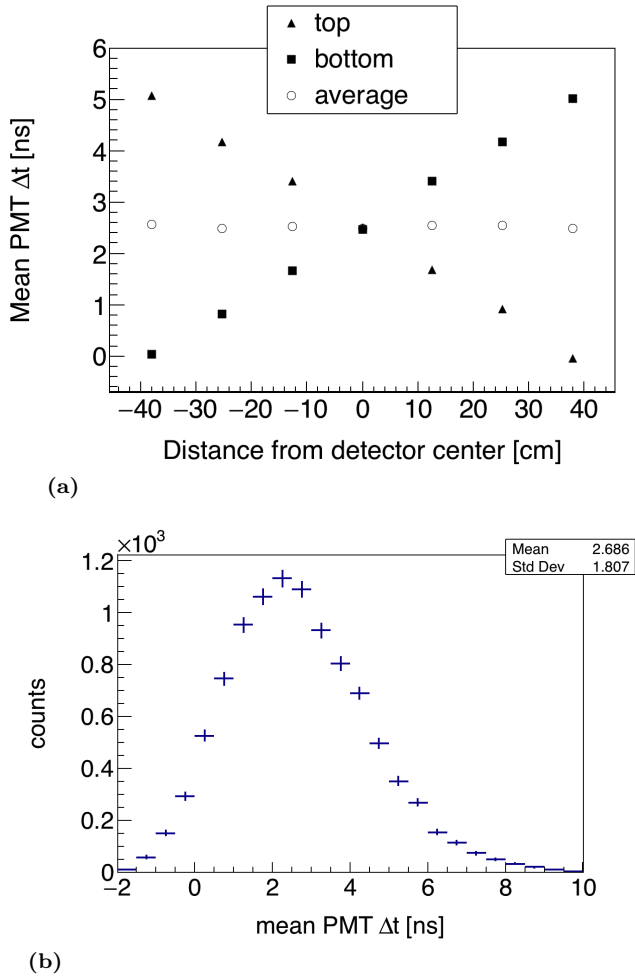


FIG. 9: A collimated ^{60}Co source is used to produce photon events with constant ToF at seven locations along the detector. ^{60}Co produces coincident photons, and one is detected by the scintillator and the other by a separate trigger detector. Δt is the timing of a PMT signal relative to a signal from the trigger detector. In (a), it can be seen that the average between signals from both PMTs does not depend on position. By using the PMT average, there is a reduction in error due to the time required for scintillation light to travel through the scintillator. The uncertainty in ToF measurements is equal to the standard deviation seen in (b), or about ± 2 ns, because all photons from the ^{60}Co source have the same ToF.

where $t_{\text{avg}}^{\text{PMT}s}$ is the average of the times of signals from both PMTs of a scintillator, t_{beam} is the time of a signal provided by the accelerator at the beginning of each pulse, and C is a constant timing offset. Any process that produces a timing delay that does not change from pulse to pulse contributes to C . For example, the time required for photons to travel from the bremsstrahlung radiator to the target, the propagation of signals through the cables connecting the PMTs, delays in the electronics, etc.

The value of C , which may be different for each detector, is determined by comparing the timing spectra of the gamma flash produced by a non-neutron produc-

ing aluminum target, to that produced when no target is used. The difference between these two spectra reveals a prominent peak in the ToF spectrum due to photons that scatter from the aluminum target. These photons must travel 125 cm to reach the center of any detector and 130 cm to reach the top, for which it takes light 4.2 ns and 4.3 ns to travel, respectively. The value of C used for each detector is equal the value that places the time corresponding to the peak of the target-induced gamma flash at 4 ns.

Under the assumption that the neutrons are non-relativistic and travel directly from the target to the detectors unimpeded, the calculation of neutron energy from ToF is straightforward. The assumption that neutrons predominantly travel to the detectors unimpeded was validated by MCNP simulations examining the scattering of fission neutrons within the fission target and detector shielding. These simulations are discussed in sections II D and II A.

B. Particle Position Reconstruction

Each detector is not capable of measuring the position of a detected particle along the axes parallel to its width (15.24 cm) or depth (3.81 cm), which contributes $\pm 3^\circ$ to the total angular uncertainty. The position of a detected particle along the 76.2 cm length of the scintillator is calculated using the timing difference of signals from both of a detector's PMTs. Assuming that scintillation light travels from an initial point, let it be x cm from the center of a scintillator, to both PMTs at a velocity that is constant with respect to the scintillator's length-wise axis, then the difference between the times at which the light will reach each PMT ($\Delta t^{\text{PMT}s}$) is given by:

$$\begin{aligned} \Delta t^{\text{PMT}s} &= t^{\text{PMT}_1} - t^{\text{PMT}_2} \\ &= \frac{(L/2 + x)n_{\text{eff}}}{c} - \frac{(L/2 - x)n_{\text{eff}}}{c} \\ &= 2x \frac{n_{\text{eff}}}{c}. \end{aligned} \quad (2)$$

Solving for x gives

$$x = \frac{c}{2n_{\text{eff}}} \Delta t^{\text{PMT}s}, \quad (3)$$

where t^{PMT_1} and t^{PMT_2} are the times of signals from each of a detector's PMTs relative to the accelerator gun pulse, L is the length of the scintillator, c is the speed of light, n_{eff} is the effective index of refraction of the scintillation material. A least squares linear fit between x and $\Delta t^{\text{PMT}s}$ was performed on data gathered using coincident photons emitted by a collimated ^{60}Co source, as described in the previous section. The resulting fit parameters, seen in Fig. 10, are used to find the position of detected particles.

Using the slope of the linear fit in Fig. 10, along with Eq. 3, an effective index of refraction of the scintillation

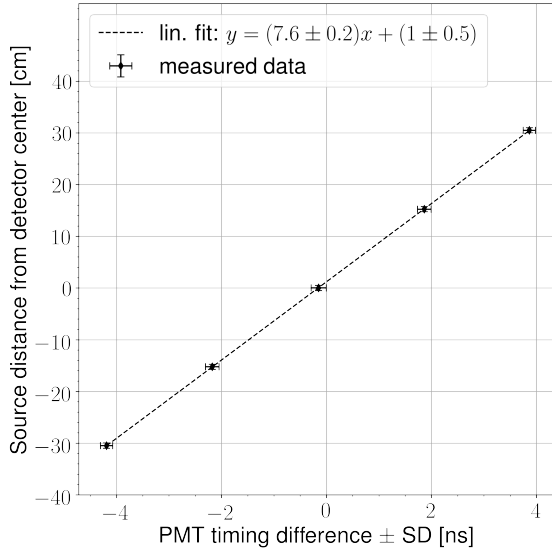


FIG. 10: A collimated ^{60}Co source is used to produce photon events at five different positions along the scintillator. The mean PMT timing difference of events at each position varies linearly with respect to the distance of the ^{60}Co source from the center of the detector. The result of a linear least squares fit to this data is used to calculate the position of detected particles along the length of each scintillator.

material is calculated to be 2.0. This index of refraction is said to be “effective” because its measurement is sensitive only to the scintillation light’s average speed projected onto the axis parallel to the scintillator’s longest dimension, which is equal to the intrinsic speed of light in the material only if the light is traveling parallel to the scintillator’s length. While the detection of scintillation light by both PMTs favors light paths which are parallel or nearly-parallel to the scintillator’s length, there is some reflection of detected scintillation light from the boundaries of the scintillator. This effect contributes to the ± 9 cm measurement uncertainty in particle position reconstruction. As a result of these effects, the index of refraction measured here is $\sim 20\%$ more than the actual value of 1.58 for PVT.

C. Measurements with ^{252}Cf

A ^{252}Cf source was placed at the center of the detection system shown in Fig 2 in order to measure the n-n opening angle distribution. Several such past measurements have been performed (see refs [8–11]), and serve as a means to validate the methods used throughout this study.

The ^{252}Cf source produces a cleaner ToF spectrum than photofission due to the lack of beam related back-

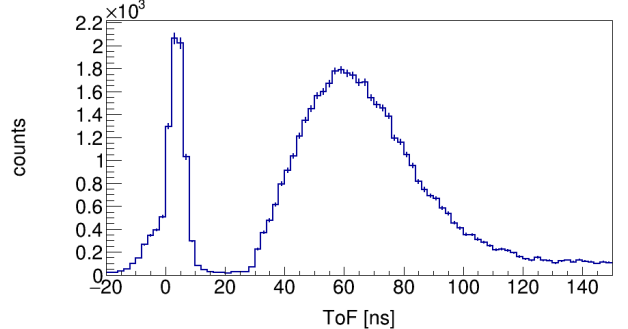


FIG. 11: Measured ToF spectrum from the SF of ^{252}Cf . The sharp peak on the left is due to fission photons, followed by another peak due to fission neutrons.

grounds (see Fig. 11), and, therefore, these measurements have a better signal to noise ratio. Also, there is no concern over the detection of accidental neutron coincidences because the fission rate of the ^{252}Cf source was about 3,500 fissions/s, making it highly unlikely that multiple fissions will occur during the electronic acceptance time window of 150 ns. The beginning of the 150 ns neutron acceptance time window was triggered by a 2-fold coincidence, within a 4 ns window, between two separate $10 \times 10 \times 5 \text{ cm}^3$ plastic scintillators, one placed above and the other below the source at a distance of 30 cm. Aside from this difference in the time window triggering mechanism, identical methods were used for both photofission and SF measurements.

IV. ANALYSIS

The efficiency and acceptance of the neutron detection system varies greatly over its opening angle range of 20° to 180° , as illustrated in Fig. 12. This is both due to the neutron detection system’s non-spherical symmetry and to varying efficiency as a function of particle position on the detector. In order to give a result that is sensitive to angular correlations, but is highly insensitive to detector efficiencies and experimental drifts in PMT voltage, accelerator current, etc., angular correlation is determined by dividing a correlated neutron distribution by an uncorrelated neutron distribution. That is,

$$\text{angular correlation} = \frac{nn_{\text{corr}}(\theta)}{nn_{\text{uncorr}}(\theta)}, \quad (4)$$

where $nn_{\text{corr}}(\theta)$ is the n-n yield after the subtraction of accidental n-n coincidences, and $nn_{\text{uncorr}}(\theta)$ is a convolved distribution of uncorrelated n-n pairs, which is produced by pairing neutron events that occurred during different pulses. The subtraction of accidental n-n coincidences to produce $nn_{\text{corr}}(\theta)$ amounts to a 10% correction, the procedure of which is covered in section IVB. The construction of $nn_{\text{uncorr}}(\theta)$ is described in detail in section IV A.

505 A. Cancelation of Detector Efficiencies, Drifts, and
 506 Geometric Phase Space

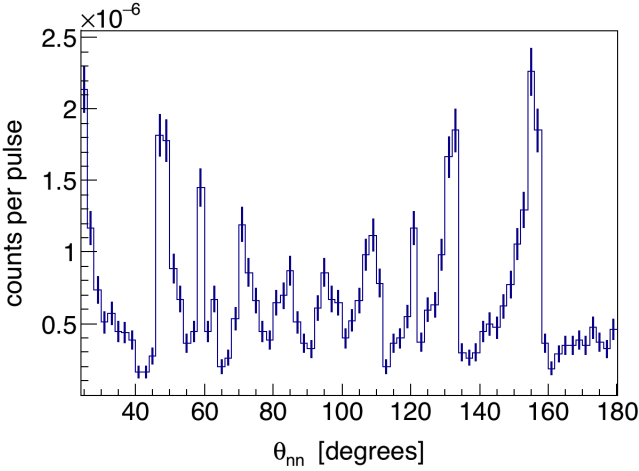


FIG. 12: Raw n-n opening angle yield from the photofission of ^{238}U . This distribution is highly influenced by the detection system's geometry and efficiency.

507 The construction of $nn_{\text{uncorr}}(\theta)$ is achieved by pairing
 508 detected neutrons that were produced during different ac-
 509 celerator pulses. The same set of pulses used for $nn_{\text{corr}}(\theta)$
 510 is used here, so each of these pulses individually consist
 511 of the detection of two coincident neutrons. When con-
 512 structing $nn_{\text{uncorr}}(\theta)$, it is desirable that the neutrons
 513 comprising each uncorrelated n-n pair originated from
 514 different pulses that occurred as closely together in time
 515 as possible. A smaller time difference between pulses
 516 that are paired for this purpose increases the chance that
 517 both neutrons were detected under the same experimen-
 518 tal conditions amid any drifting of accelerator current,
 519 PMT voltages, and varying rates of noise. However, some
 520 time difference between the pulses must be allowed so as
 521 not to cause insufficient counting statistics. Accordingly,
 522 uncorrelated n-n pairs used to construct $nn_{\text{uncorr}}(\theta)$ are
 523 formed by neutrons that were detected within 30 minutes
 524 or less of each other.

525 Uncorrelated n-n pairs will have a slightly different
 526 joint energy distribution than correlated n-n pairs, which
 527 could affect the extent to which the effects of detector
 528 efficiency cancel in Eq. 4. This issue is addressed in sec-
 529 tion V A, where it is shown that these differences have
 530 little potential to significantly affect the final result.

531 Figure 13(a) shows the measured yield distribution of
 532 correlated neutrons, $nn_{\text{corr}}(\theta)$, from the photofission of
 533 ^{238}U . The structure seen here is reflective of the under-
 534 lying n-n angular correlations as well as the geometric
 535 acceptance and efficiencies of the neutron detectors. Fig-
 536 ure 13(b) reveals how a clear picture of n-n angular corre-
 537 lations emerges when taking the ratio between $nn_{\text{corr}}(\theta)$
 538 and $nn_{\text{uncorr}}(\theta)$.

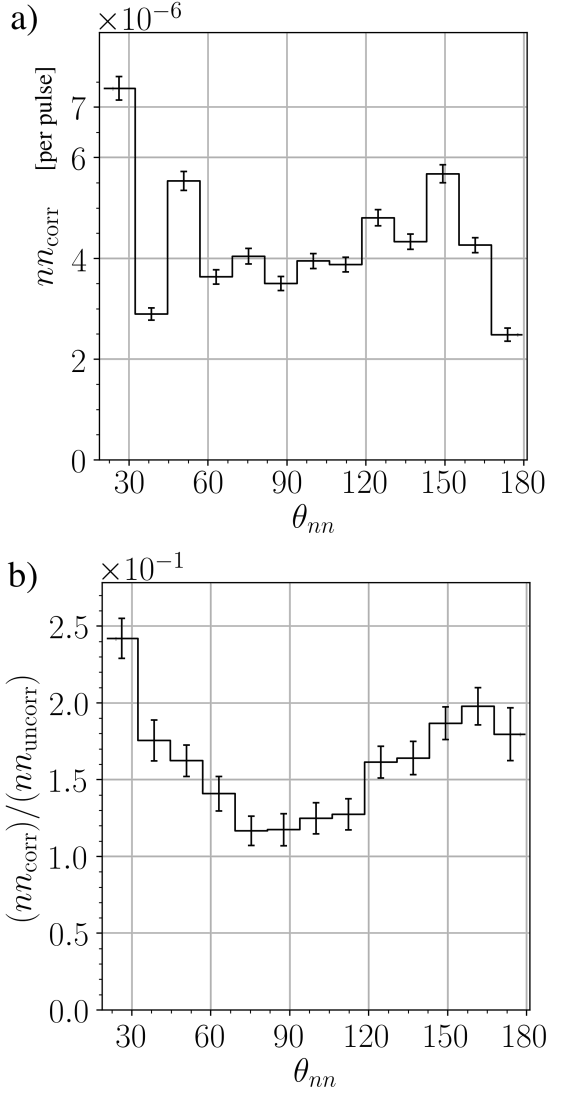


FIG. 13: (a) n-n opening angle distribution from the photofission of ^{238}U before normalization, and, (b) after normalizing to the distribution of uncorrelated n-n events from different pulses. All measured neutrons have an energy greater than 0.4 MeV.

540 B. Subtraction of Accidental Coincidences

541 The observation of two uncorrelated signals in the neu-
 542 tron ToF range, whether caused by neutrons, photons,
 543 or noise, is referred to as an *accidental coincidence*. Ac-
 544 cidental coincidences due to noise and photons, which
 545 are estimated using a non-neutron producing aluminum
 546 target (see Fig. 14), amount to about 3% of all coin-
 547 cidences. Accidental coincidences due to neutrons are
 548 minimized by adjusting the accelerator's current so that
 549 there are, on average, less than 1.0 fission per accelerator

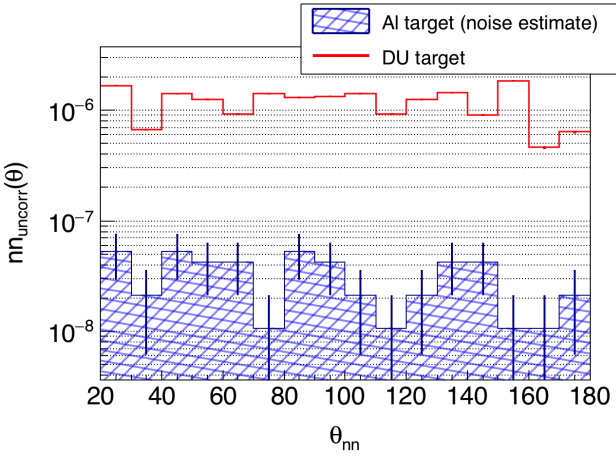


FIG. 14: An Al target was designed to scatter the same number of photons as the ^{238}U target, thus serving as an equivalent non-neutron producing target well-suited for noise estimates. The rate of the detection of coincident events in the neutron ToF range while using the Al target was 3% that of the ^{238}U target. Thus, 3% of coincident events used in the determination of n-n angular correlations in ^{238}U can be attributed to noise.

550 pulse, nevertheless, statistical fluctuations in the number 551 of fissions per pulse result in the production of acci- 552 dental coincident neutrons that originated from different, 553 and therefore, uncorrelated fissions. There are also ac- 554 cidental neutron coincidences caused by the occurrence 555 of multiple (γ, n) reactions in a single pulse. The energy 556 integrated (γ, n) cross-section of ^{238}U , weighted by the 557 bremsstrahlung energy distribution, is about a factor of 558 5.5 times greater than it is for photofission (see Fig. 15). 559 As a result, the raw n-n coincident yield will contain a sig- 560 nificant number of n-n coincidences from multiple (γ, n) 561 reactions in relation to n-n coincidences from fission. The 562 presence of accidental n-n coincidences has the effect of 563 washing out the signal from correlated neutrons.

564 The raw measurement of n-n yield consists of a mix of 565 correlated and accidental neutron coincidences, that is

$$nn_{\text{raw}}(\theta_{nn}) = nn_{\text{corr}}(\theta_{nn}) + nn_{\text{acc}}(\theta_{nn}), \quad (5)$$

588 where $nn_{\text{raw}}(\theta_{nn})$ and $nn_{\text{acc}}(\theta_{nn})$ are the per-pulse n-n 589 yields as a function of opening angle, θ_{nn} , for all detected 590 n-n pairs, and detected accidental n-n pairs, respectively. 591 As already defined, $nn_{\text{corr}}(\theta_{nn})$ is the per-pulse yield of 592 detected correlated n-n pairs.

593 Because the n-n coincidences comprising $nn_{\text{acc}}(\theta_{nn})$ 594 consist of two independent detected neutrons, they are 595 governed by the exact same physics and are subject to 596 the exact same experimental conditions as n-n coinci- 597 dences formed by pairing of single neutrons that were 598 detected during different pulses. Therefore, the open- 599 ing angle distribution formed by pairing neutrons that 600 were detected during different pulses, denoted $nn_{dp}(\theta_{nn})$, 601 is proportional to $nn_{\text{acc}}(\theta_{nn})$. $nn_{dp}(\theta_{nn})$ is constructed 602 from the set of all possible pulse-pairs formed by pulses

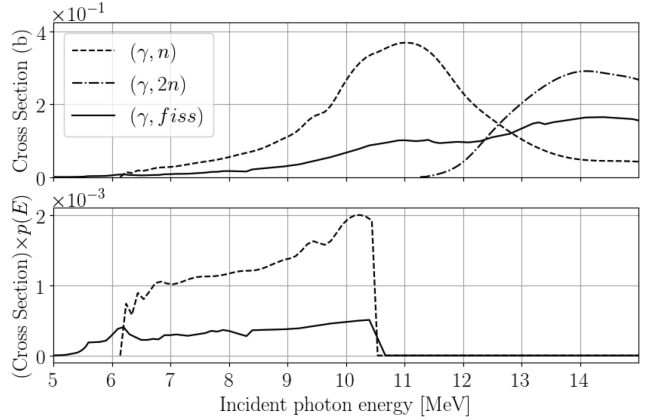


FIG. 15: (top) ENDF cross-sections of (γ, fiss) , direct (γ, n) , and direct $(\gamma, 2n)$. (bottom) Cross-sections weighted by the simulated relative rate of bremsstrahlung photons that reach the target as a function of photon energy. The integrated cross-sections of (γ, n) is 5.5 times greater than for (γ, fiss) .

583 that occurred within 0.2 seconds of each other. The re- 584 striction in time difference is applied in order to increase 585 the chance that pulse pairs together occurred under simi- 586 lar experimental conditions. There are no other restric- 587 tions on which pulses can be used in this case. Thus, many 588 pulse-pairs used for the construction of $nn_{dp}(\theta_{nn})$ will 589 contain no detected neutrons.

590 While $nn_{dp}(\theta_{nn})$ and $nn_{\text{acc}}(\theta_{nn})$ are proportional, 591 $nn_{\text{acc}}(\theta_{nn})$ is not equal to $nn_{dp}(\theta_{nn})$, because there are, 592 on average, more detected neutrons per pulse-pair than 593 per pulse. As the following analysis shows, $nn_{\text{acc}}(\theta_{nn}) =$ 594 $\frac{1}{2}nn_{dp}(\theta_{nn})$, under the condition that $nn_{\text{acc}}(\theta_{nn})$ is nor- 595 malized to the number of pulses and $nn_{dp}(\theta_{nn})$ to the 596 number of pulse-pairs looked at. When looking at single 597 pulses, the probability of there being a detected uncorre- 598 lated n-n pair is denoted by P_{sp}^{n-n} , and when looking at 599 pulse-pairs, by P_{dp}^{n-n} . Thus, P_{sp}^{n-n} and P_{dp}^{n-n} determine the 600 relative rates of $nn_{\text{acc}}(\theta_{nn})$ and $nn_{dp}(\theta_{nn})$, respectively.

601 The statistics of the detected uncorrelated neu- 602 trons per pulse is assumed to follow a Poisson distribu- 603 tion, which describes the occurrence of independent ran- 604 dom events. Accordingly, the probability of the detection 605 of k uncorrelated neutrons in a given pulses is

$$p(k) = \frac{e^{-\lambda} \lambda^k}{k!}, \quad (6)$$

606 where λ represents the mean number of uncorrelated de- 607 tected neutrons per pulse. In principle, λ equals the total 608 number of detected uncorrelated neutrons divided by the 609 total number of pulses. Determination of λ cannot be 610 done in practice, because one would need to know which 611 pairs of detected neutrons are correlated. However, the 612 largest possible value for λ is the total number of de- 613 tected neutrons divided by the total number of pulses, as 614 this quantity counts all detected neutrons, whether they 615 are correlated or uncorrelated. For this work, that places

an upper bound on λ of 5.5×10^{-3} detected uncorrelated neutrons per pulse, which is small enough to truncate all terms beyond the leading term in the following analysis.

Because $P_{\text{sp}}^{\text{n-n}}$ represents the probability of the detection of two uncorrelated neutrons in a single pulse, $P_{\text{sp}}^{\text{n-n}}$ is equal to $p(2)$, as per Eq. 6. Thus,

$$\begin{aligned} P_{\text{sp}}^{\text{n-n}} &= \frac{e^{-\lambda} \lambda^2}{2!} \\ &\approx \frac{\lambda^2}{2} + \mathcal{O}(\lambda^3). \end{aligned} \quad (7)$$

When considering the case of $P_{\text{dp}}^{\text{n-n}}$, recall that, in this case, uncorrelated n-n pairs are formed by examining pulse-pairs. Here, an uncorrelated n-n pair occurs when there is a detected neutron in both pulses. Because all terms beyond the leading term are being truncated, pulse-pairs in which one or both of the pulses comprise two or more detected neutrons do not need to be considered. Thus, $P_{\text{dp}}^{\text{n-n}}$ is equal to the probability of there being exactly one detected neutron in each pulse, which is the square of the probability of there being exactly one detected neutron in a single pulse, namely, $p(1)^2$. Thus, again using Eq. 6,

$$\begin{aligned} P_{\text{dp}}^{\text{n-n}} &= (e^{-\lambda} \lambda)^2 \\ &\approx \lambda^2 + \mathcal{O}(\lambda^3). \end{aligned} \quad (8)$$

Because $P_{\text{dp}}^{\text{n-n}}$ and $P_{\text{sp}}^{\text{n-n}}$ determine the relative rates of $nn_{\text{dp}}(\theta_{nn})$ and $nn_{\text{acc}}(\theta_{nn})$, respectively, and because the two distributions have the same shape, from Eq.'s (8) and (7), it follows that

$$nn_{\text{acc}}(\theta_{nn}) = \frac{1}{2} nn_{\text{dp}}(\theta_{nn}). \quad (9)$$

Finally, from Eq.'s 9 and 5, the distribution of solely correlated n-n pairs can be recovered from the raw measurement as follows

$$nn_{\text{corr}}(\theta_{nn}) = nn_{\text{raw}}(\theta_{nn}) - \frac{1}{2} nn_{\text{dp}}(\theta_{nn}). \quad (10)$$

V. POTENTIAL SOURCES OF ERROR

A. Correlated *versus* uncorrelated n-n energy distribution

In order to effectively minimize the dependence of the result on detector geometry/efficiency, the numerator and denominator of Eq. 4 must comprise neutron pairs with a similar energy distribution. Note that accidental coincident neutrons from (γ, n) are completely removed from $nn_{\text{corr}}(\theta)$, the numerator in Eq. 4, by the subtraction of accidental coincidences, but are not removed from the denominator, $nn_{\text{uncorr}}(\theta)$. This is the reason for using only pulse-pairs that have two events in each pulse when determining the uncorrelated neutron distribution.

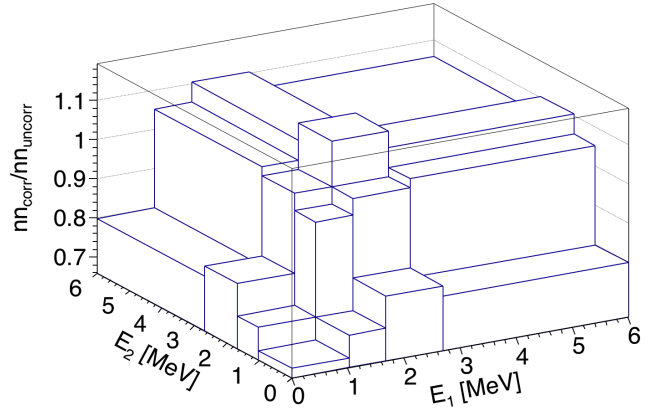


FIG. 16: The z-axis represents the ratio between the correlated and uncorrelated rates of binned n-n energies. The energy bins are chosen such that each contains an equal number of events, or 1/16th of the total events.

Doing so increases the selection of neutrons from fission as opposed to (γ, n) .

When examining differences between the neutron energy distributions in $nn_{\text{corr}}(\theta)$ and $nn_{\text{uncorr}}(\theta)$, it is important to consider how the energies of both neutrons forming n-n pairs vary together, or, in other words, their joint energy distribution. Fig. 16 shows the ratio between the rates for correlated and uncorrelated n-n pairs of various binned energies. The effect that these discrepancies in energy distribution have on the final result can be examined by applying a weighting factor to each event in $nn_{\text{uncorr}}(\theta)$ such that a recalculation of the result in Fig. 16 produces a flat curve. A comparison of the determined angular correlation with and without the application of these weighting factors to all uncorrelated n-n events is seen in Fig. 17. The resulting differences in angular correlation are negligible.

B. Detector Cross-talk

Cross-talk occurs when, after a particle is detected once, the same particle, by any means, causes a detection to be registered in a different detector. For example, upon detection, a particle may undergo elastic scattering and then travel into another detector where it is detected again, or, it may produce secondary particles that are detected. The two coincident detections of a cross-talk event are causally correlated, and thus they have the potential to contaminate the signal from correlated fission neutrons. If both detections occur during the ToF range typical for fission neutrons, then the cross-talk event cannot be distinguished from the detection of two correlated neutrons.

Recent works that measured the n-n angular correlations in the spontaneous fission of ^{252}Cf and ^{240}Pu [9, 13] addressed this effect by using an MCNP-PoLiMi simulation to estimate and then subtract cross-talk from their

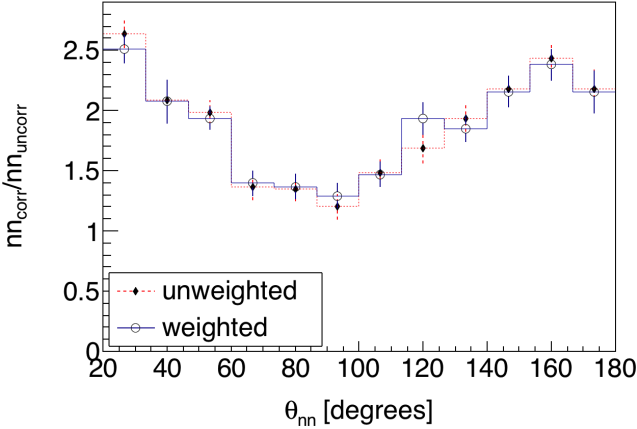


FIG. 17: Each uncorrelated n-n event can be weighted such that the weighted histograms of the joint n-n energy distributions of correlated and uncorrelated n-n pairs are equal. Comparison of the calculated angular correlation results, with and without such weighting factors applied to all uncorrelated n-n events, illustrates that any effects due to the discrepancies in the joint energy distributions of correlated and uncorrelated n-n pairs are negligible.

measurements. In this work, the issue of cross-talk is approached differently by employing the use of detector shielding aimed at reducing cross-talk to a negligible rate. By using shielding to reduce cross-talk, this measurement is less dependent on the details of the models used by MCNP-PoLiMi to simulate neutron transport and detection. MCNP-PoLiMi simulations are used in this work only to verify that the effect of cross-talk is negligible.

The scintillators used here are much larger than those used in similar works, such as in refs [9, 13], allowing them to be placed much farther from the fission source without causing a ruinous loss in coincidence rates. An increase in the distance between the detectors and the fission source makes this measurement less sensitive to angular uncertainty, which depends directly on the uncertainty in the position of a detected particle due to, for example, the scattering of neutrons from detector shielding. For this reason, larger amounts of shielding can be used without concern of introducing large errors.

Furthermore, the geometry of the neutron detection system makes it kinematically impossible for a neutron to undergo a single scattering event with a proton in one detector, which is the basis for scintillation, and then travel directly into another detector with enough kinetic energy to be detected a second time. For this reason, upon being detected, a neutron must scatter from one or more intermediate nuclei, such as lead or carbon, in order for it to reach another detector with enough energy to be detected again. This fact follows from the conservation of energy and momentum. In order to support the claim that the design of the neutron detection system reduced cross-talk to negligible rates, a detailed MCNP-PoLiMi [15] simulation was performed in which a built-in ^{252}Cf source is positioned at the center of a model of the

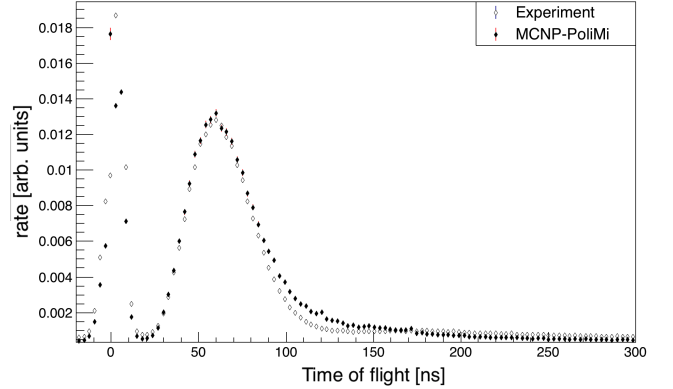


FIG. 18: Measured *versus* simulated ToF spectrum from the SF of ^{252}Cf . The simulation used the detector response model outlined in ref [16]. The simulated and measured curves are normalized in order to facilitate comparison.

725 neutron detection system.

1. Simulation of Detector Cross-talk

726 The cross-talk simulation included all scintillators, 727 shielding, detector supporting structures, and the concrete walls surrounding the experimental cell. MCNP- 728 PoliMi's built-in ^{252}Cf spontaneous fission source was 729 used, which emits neutrons with the correct correlations 730 and multiplicities according to previous measurements. 731 Detector response was modeled using a program included 732 with the MCNP-PoliMi distribution called MPPost [16]. 733 The model is based on the electron equivalent light output 734 (MeVee) produced by particles as they undergo collisions 735 with carbon and hydrogen within organic plastic 736 scintillators. A minimum deposited energy of 0.4 MeV 737 (equivalent to 0.05 MeVee for neutrons) was assumed for 738 detectable particles, which was chosen because the neutron 739 detection system exhibited a sharp decline in detection 740 efficiency for neutrons below 0.4 MeV.

741 For neutron collisions with hydrogen, the light output 742 in MeVee, denoted L , is calculated by the following empirically derived formula [16]

$$L = 0.0364\Delta E_n^2 + 0.125\Delta E_n,$$

743 where ΔE_n is equal to the loss in the kinetic energy of the 744 neutron due to the collision. Neutron interactions with 745 carbon are assumed to generate a small light output of

$$L = 0.02\Delta E_n.$$

746 As seen in Fig. 18, this model of the detection process 747 produces a ToF spectrum for the SF of ^{252}Cf that is in 748 good agreement with the measurement.

749 Figure 19 shows the distribution of cross-talk events 750 and true n-n coincidences as a function of reconstructed 751 opening angle. It is worth noting that, according to this

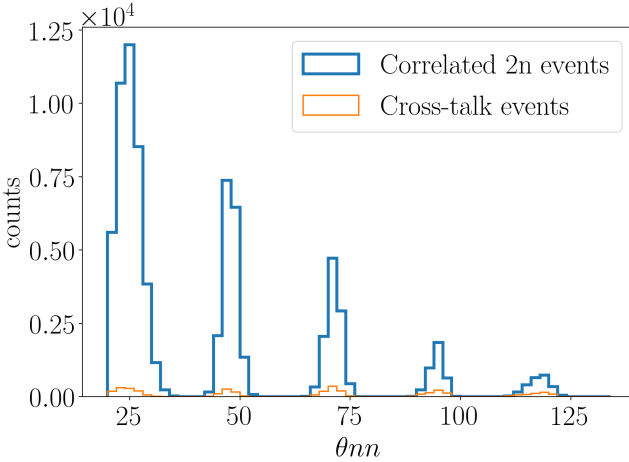


FIG. 19: MCNP-PoLiMi simulation of the number of cross-talk events *versus* correlated n-n events as a function of reconstructed opening angle. Cross-talk accounted for 3% of total events. Simulated cross-talk events do not occur primarily at small angles, but are instead spread out over a wide range of angles. Any cross-talk occurring at angles larger than 125° will be removed from the experimental data by the cuts applied to neutron ToF.

756 simulation, the effect of cross-talk is not only small, but is
 757 also distributed over a wide range of angles rather than
 758 being concentrated around 0 degrees as one might ex-
 759 pect. Angles greater than 125 degrees are not shown
 760 in Fig. 19 because cross-talk events at large angles can
 761 be readily identified in analysis due to the large amount
 762 of time required for a neutron to travel these distances.
 763 The simulation was initially performed with 5 cm of lead
 764 shielding placed behind the scintillators, and the num-
 765 ber of cross-talk events accounted for 11% of the total
 766 coincident neutron events. This value fell to 3% when
 767 polyethylene was used instead of lead, motivating the
 768 placement of 10 cm of polyethylene behind the detectors
 769 instead of lead.

771 C. Neutron Scattering within the Target

772 A potential source of error in opening angle measure-
 773 ments is the scattering of emitted neutrons as they tra-
 774 verse the fission target. This is a cause for concern be-
 775 cause when neutrons scatter from heavy nuclides such
 776 as ^{238}U , they are likely to be deflected at large angles
 777 resulting in n-n opening angles that do not reflect the
 778 true underlying fission kinematics. The effect that this
 779 has on this work is assessed by MCNP simulations. In
 780 summary, for 6% of n-n pairs, at least one neutron out
 781 of the two scatters before exiting the target, according to
 782 the simulation. This effect does not have a large influ-
 783 ence on the measured θ_{nn} distribution according to the
 784 simulation data shown in Fig. 21.

785 The rate of elastic scattering is affected by the size
 786 and shape of the target. A thin strip is the ideal target

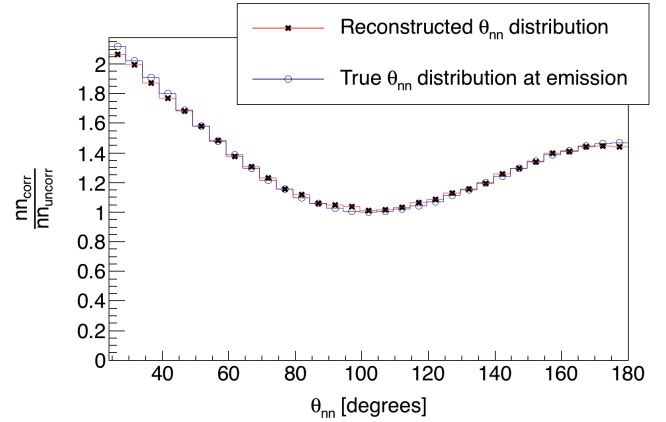


FIG. 20: MCNP-PoLiMi simulation of correlated ^{252}Cf neutrons sampled uniformly throughout a $0.05 \times 2 \times 4 \text{ cm}^3$ U-238 target. The slight difference between the curves is due solely to the elastic scattering of neutrons within the target, since detector physics was not simulated. In the reconstructed θ_{nn} distribution (\star), only neutrons which enter a physical volume at which a detector was located during the experiment are counted. The true θ_{nn} distribution at the moment of emission is also plotted (\circ).

787 shape regarding the rate of neutron elastic scattering per
 788 unit of total target volume. See Fig 20 for the simulated
 789 elastic scattering rates for both thin strip and cylindrical
 790 shaped targets. The simulation indicated that the rate of
 791 elastic scattering in cylindrical targets is about a factor
 792 of two times greater than in thin strip targets with the
 793 same volume.

794 The target's dimensions are small enough that the
 795 rate of photon absorption, and thus photo-neutron pro-
 796 duction, is virtually uniform throughout the entire tar-
 797 get volume. An MCNP-PoLiMi simulation was used
 798 to generate ^{252}Cf spontaneous fission events uniformly
 799 throughout the target. The SF of ^{252}Cf is used instead
 800 of the photofission of ^{238}U because of the current lack
 801 of photofission models, however, the underlying fission
 802 kinematics are, broadly speaking, the same for the SF
 803 of ^{252}Cf and the photofission of ^{238}U , thus, the two pro-
 804 cesses have similar n-n correlations.

805 Section VIB discusses the observation of an unex-
 806 pected drop in correlation around 180° in our photofis-
 807 sion of ^{238}U measurement, as seen in Figs. 22 and 23.
 808 This motivated a second simulation regarding elastic
 809 scattering which examined whether this decrease in the
 810 correlation around 180° opening angles reflects the un-
 811 derlying physics of the fission process. In particular, note
 812 that throughout these measurements, the target was con-
 813 tinuously rotated once per 8 seconds. This means that for
 814 the determination of the uncorrelated opening angle dis-
 815 tribution, the trajectories of the two neutrons were taken
 816 from two different pulses in which the target was at a dif-
 817 ferent orientation for each of them. Additionally, each of
 818 the neutrons likely originated from different regions of the
 819 target volume. On the other hand, for the same-pulse,

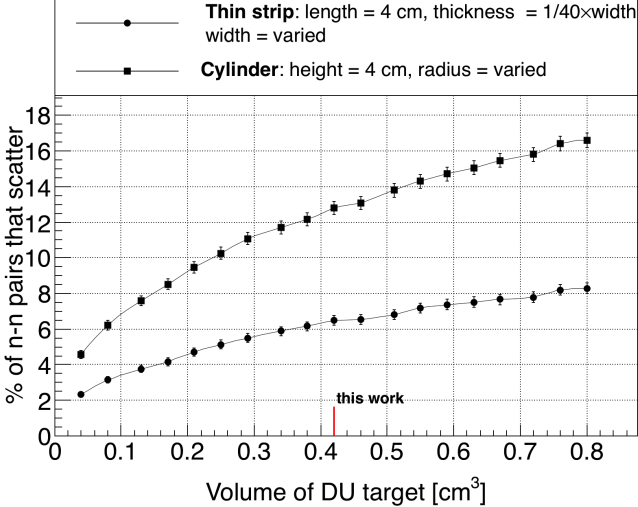


FIG. 21: Result of an MCNP simulation in which n-n pairs, with energies sampled from a typical watt fission spectrum, were generated uniformly throughout the volume of DU targets. The y-axis is the rate of opening angle contamination due to the scattering of, within the DU target in which they were produced, either one or both of a pair of neutrons. The lack of symmetry of a thin strip target can be removed by slowly rotating the target around the vertical axis during data acquisition, making it the optimal target geometry for the minimization of the rate of neutron scattering. The target used in this work had a length of 4 cm, a width of 2 cm, and a thickness of 0.05 cm.

correlated neutron measurement, the target was in the same orientation and the two neutrons were generated at the same position in the target. For these reasons, the rates of neutron scattering within the target are not necessarily equal for the same-pulse and different-pulse cases. As such, we investigated whether these differences could cause this apparent decrease in the opening angle distribution.

Using the correlated ^{252}Cf SF source built-in to MCNP-PoLiMi, the opening angle distribution of neutrons at the moment of emission, labeled *true* in Fig. 21, were compared to that the neutrons after they have escaped the target, labeled *reconstructed* in Fig. 21. The location of fission events were sampled uniformly throughout the targets volume. The analysis employs the same technique outlined in section IV A, in which a correlated neutron distribution is divided by an uncorrelated neutron distribution. The correlated neutron distribution is formed by pairing neutrons emitted during the same fission, and the uncorrected distribution by the pairing of neutrons emitted during different fissions. In order to account for the effect of a rotating target on the trajectories of neutrons from different-pulses, the coordinate system was rotated about the vertical axis accordingly for different fission events. The result from this simulation suggests that the rotating $0.05 \times 2 \times 4 \text{ cm}^3$ U-238 target does not, due to neutron scattering, result in a significant departure from the true n-n opening angle distribution.

VI. RESULTS

The n-n opening angle correlation is calculated using the methods outlined in sec IV, in which a correlated neutron yield is divided by an uncorrelated yield. The results are compared with output from FREYA [17] (Fission Reaction Event Yield Algorithm), which was developed by the collaborative efforts of researchers from Lawrence Berkeley National Laboratory, Lawrence Livermore National Laboratory, Los Alamos National Laboratory, and University of Michigan Nuclear Engineering, and has been included in MCNP beginning with version 6.2 .

The most recent release of FREYA (version 2.0.3) does not model photofission directly, but instead uses a neutron-induced fission model to approximate photofission [18]. For a given nucleus with Z protons and A total nucleons, the code selects the neutron-induced fission model for a $Z(A-1)$ nucleus, and chooses an incident neutron energy such that the compound ZA nucleus will have, relative to ZA's ground state, an excitation energy that is equal to the energy of the would-be incident photon.

When using FREYA to model photofission in this work, all model parameters, such as level density and partition parameters, were set to their default values for neutron-induced fission. FREYA was told to use the fission fragment mass distribution, $Y(A)$, and the average total kinetic energy, $\langle \text{TKE} \rangle(A)$, from the ^{238}U photofission measurements described in ref [19]. In ref [6], the authors warn that using FREYA in this way to model photofission is only an approximation and could lead to incorrect results. Nonetheless, FREYA is used here as such because it is the only photofission model available to the authors of the present work.

A. n-n angular correlation *versus* neutron energy

The measured θ_{nn} distribution from the photofission of ^{238}U and the SF of ^{252}Cf are presented with the following two different types of cuts applied to the energies of neutrons in coincidence: in Figs. 22 (^{238}U) and 24 (^{252}Cf), a minimum energy threshold is applied to both neutrons, and in Figs. 23 (^{238}U) and 25 (^{252}Cf), the energy of both neutrons are required to fall within a specified range

When using a histogram to estimate a continuous distribution from the relatively small number of data points obtained in this work, one faces the following dilemma: small bins produce histograms with large uncertainties that are dependent on the chosen bin-width, while large bins obscure potentially useful information. For this reason, kernel density estimates (KDE) with 68% confidence intervals are plotted alongside histograms. A KDE is a method for estimating a continuous probability distribution from a finite set of sampled data points. The kernel was chosen to be the measurement errors in opening angle as determined by a study using coincident photons

from a ^{60}Co source, which was placed at different locations along a detector. The measurement errors in θ_{nn} are well-described by a gaussian with a standard deviation of 6° . Mathematical details of the KDE method used in this work are outlined in ref [20].

Plotted alongside each measurement is the result of a FREYA simulation. For the measurement of ^{238}U photofission, there were a total of 2,952 n-n coincident events after the subtraction of accidentals, and for the SF of ^{252}Cf , there were 21,882.

914 B. Considering θ_{abs}

915 While these results are consistent with the effect of the
916 kinematic focusing of the neutrons due to the recoil of the
917 fission fragments, the data show a small but statistically
918 significant decrease in the n-n opening angle correlation
919 in the region from about 165° to 180° , which can be seen
920 in Figs. 13 and 27, as well as in Figs. 22 and 23. This
921 feature is not evident in previous work on spontaneous
922 and neutron induced fission. The effect is particularly
923 strong for the neutron energy cuts being applied in the
924 upper right plots of both Figs. 22 and 23. A comparison

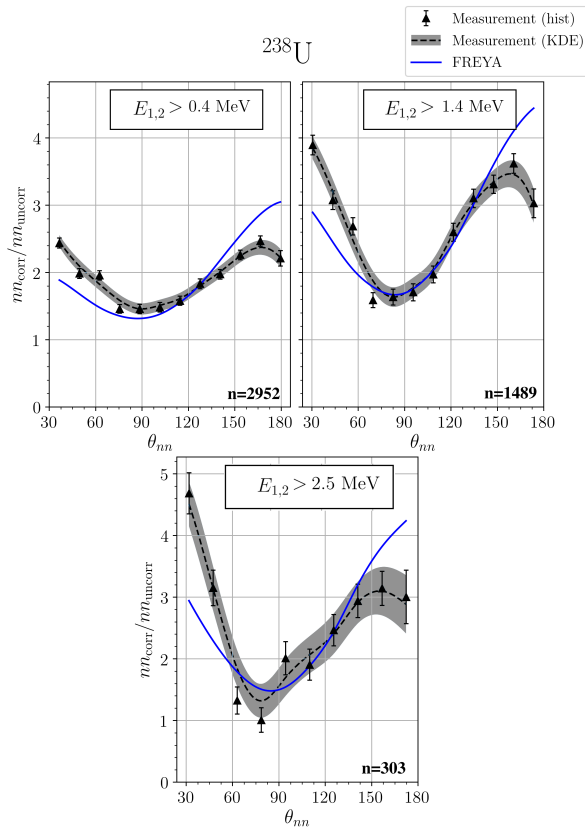


FIG. 22: θ_{nn} distribution with minimum energy threshold cuts applied to all neutrons. The number of events contributing to each plot, n , is shown. Note that the bottom plots of this figure and Fig. 23 are identical.

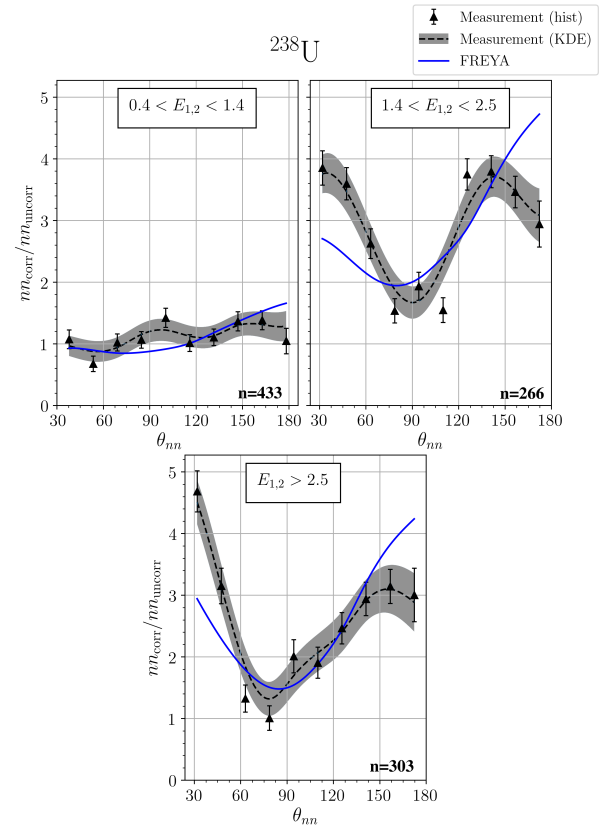


FIG. 23: θ_{nn} distribution with cuts requiring that the energy of both coincident neutrons be within the specified range. The number of events contributing to each plot, n , is shown. Note that the bottom plots of this figure and Fig. 22 are identical.

925 of the observed decrease after 160 degrees with the null
926 hypothesis that the true distribution remains constant
927 after 160 degrees yields a p-value of 0.01. This indicates
928 a 1% probability of obtaining data as compatible with
929 the above hypothesis as the data we observed. A similar
930 effect appears in the results reported in ref [12] for the
931 thermal neutron-induced fission of ^{233}U and ^{235}U , but
932 not for the spontaneous fission of ^{252}Cf or the neutron-
933 induced fission of ^{239}Pu .

934 As previously discussed in section I, photofission dif-
935 fers from spontaneous and neutron induced fission in that
936 the fission fragments for the photon-induced reaction ex-
937 hibit an asymmetry in their angle of emission, with the
938 most likely orientation of the fission axis lying perpendic-
939 ular to the direction of the incident photon. With this
940 in mind, the following series of angular cuts were made
941 on the data. Fig. 26 shows the distributions of absolute
942 opening angles of the n-n events for three different cuts
943 on the value of the n-n opening angle. For n-n open-
944 ing angles between 120° and 160° , there is an increased
945 preponderance of both neutrons being emitted around
946 90° , consistent with the interpretation of kinematic fo-
947 cusing of neutrons coming from fission fragments which
948 are themselves being emitted preferentially at 90° . How-

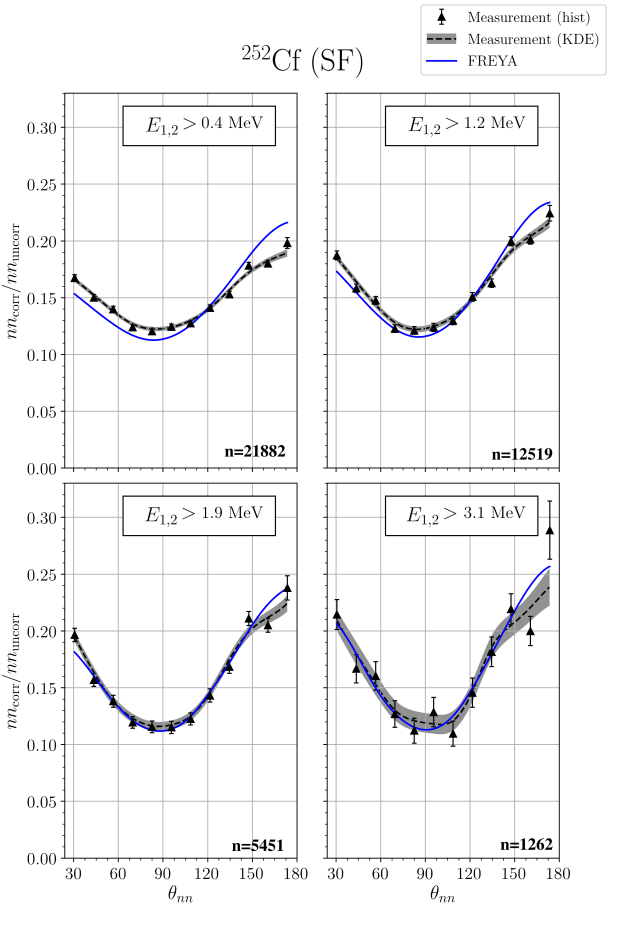


FIG. 24: θ_{nn} distribution after minimum energy threshold cuts applied to all neutrons. The number of events contributing to each plot, n , is shown. Note that the lower right plots of this figure and Fig. 25 are identical.

ever, in the opening angle region where the n-n correlation is reduced, from about 160° to 180° , this feature is less prominent.

Furthermore, if one plots the opening angle distributions for the case in which at least one neutron is emitted perpendicular to the incident photon *versus* the case in which neither neutron is emitted perpendicular to the incident photon (Fig. 27), one sees distinct differences. The fact that there are overall differences is not surprising, because in one case (Fig. 27 solid line) at least one neutron preferentially receives a kinematic boost from a fission fragment and in the other case (Fig. 27 dotted line) neither neutron does. However, the fact that the n-n correlation is reduced at 180° in opening angle when at least one of the neutrons is emitted along the preferred fission axis is unexpected. This is a feature which does not seem to appear in either neutron-induced fission, previous measurements on spontaneous fission, or our present measurement on spontaneous fission. The photo-fission of the even-even ^{238}U nucleus seems to be

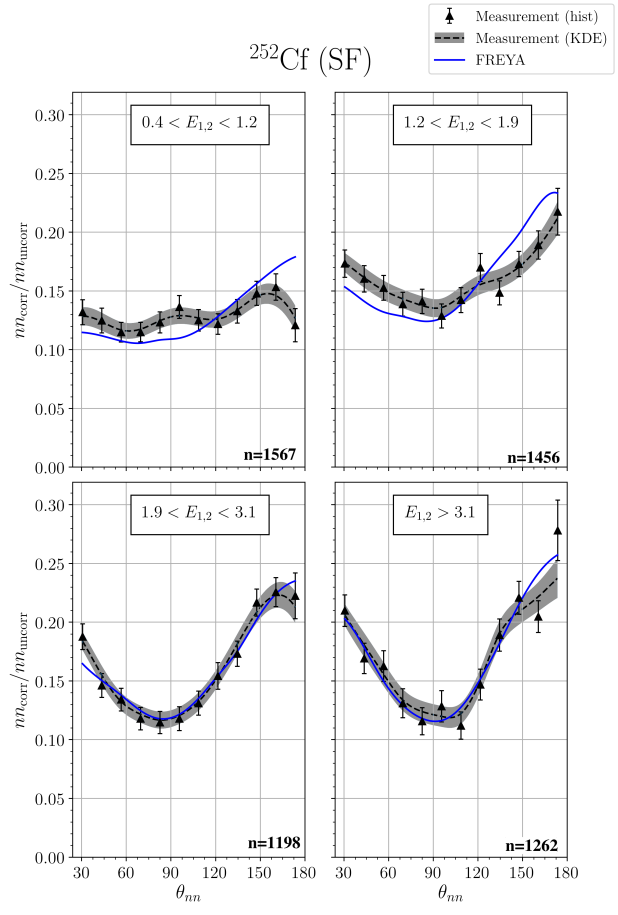


FIG. 25: θ_{nn} distribution with cuts requiring that the energy of both coincident neutrons be within the specified range. The number of events contributing to each plot, n , is shown. Note that the lower right plots of this figure and Fig. 24 are identical.

unique in this regard. The attribution of this effect to the geometric coverage of the neutron detection system or to neutron elastic scattering within the target was ruled out using simulations, as discussed in section V C.

These data are consistent with two possible explanations relating to the unique feature of the asymmetric angular emission of fission fragments in photo-fission. First, it is possible that there is a decrease in neutron emission along the fission axis. Second, the neutrons may indeed be emitted isotropically in the rest frame of the fission fragment, but one fragment essentially shadows the neutrons emitted from the other fragment, either through absorption or scattering. If it is the later case, then this effect has the potential to shed light on the time dependence of neutron emission, since shadowing would likely depend on the fission fragment separation. A definitive interpretation of this decreased n-n correlation for large opening angles in photo-fission requires further study.

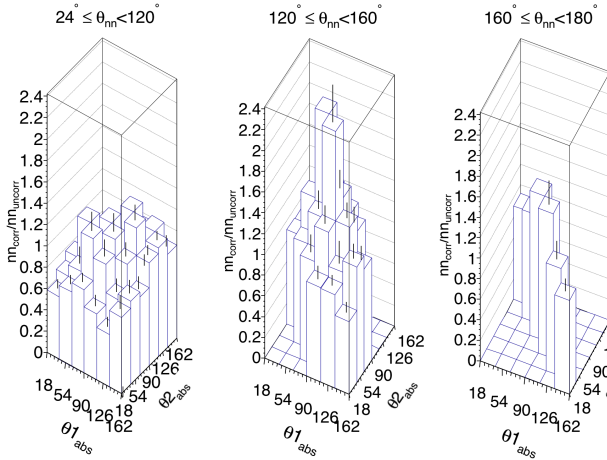


FIG. 26: Correlation is shown between the angles of each neutron with respect to the incident photon beam, denoted by θ_{1abs} and θ_{2abs} . Empty bins exist because of intrinsic geometrical phase-space.

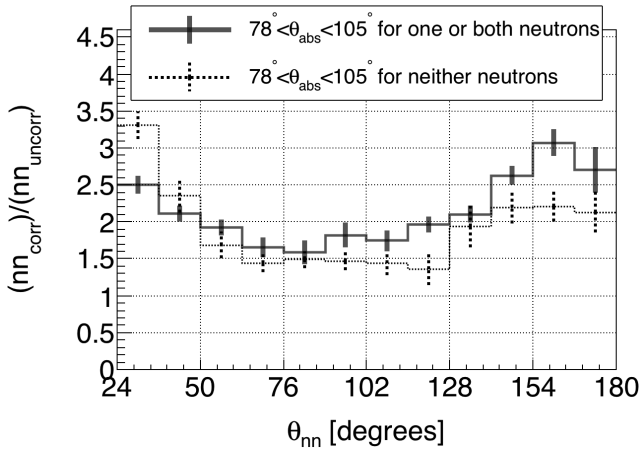


FIG. 27: Requiring that at least one of the coincident neutrons be emitted nearly perpendicular to the photon beam (solid line) produces an opening angle distribution that is different from that produced when it is required that both neutrons are emitted nearly parallel to the photon beam (dotted line).

987

VII. CONCLUDING REMARKS

988 Neutron-neutron angular correlations in the photofission of ^{238}U were measured using 10.5 MeV end-point
989 bremsstrahlung photons produced via a low duty factor,
990 pulsed linear electron accelerator. The measured angular
991

992 correlations reflect the underlying back-to-back nature of
993 the fission fragments. The method of analysis used a sin-
994 gle set of experimental data to produce a opening an-
995 gle distribution of correlated and uncorrelated neutron
996 pairs. A ratio is taken between these two sets to provide
997 a self-contained result of angular correlations, in that
998 the result is independent of neutron detector efficiencies.
999 Neutron-neutron angular correlation measurements were
1000 also made using neutrons from the spontaneous fission of
1001 ^{252}Cf and show good agreement with previous measure-
1002 ments.

1003 Measured n-n opening angle correlations in the
1004 photofission of ^{238}U do not agree very well with simula-
1005 tions using FREYA version 2.0.3, which uses a neutron-
1006 induced model to approximate photofission. These data
1007 will be useful for fine-tuning the photofission models that
1008 will be incorporated into future versions of FREYA.

1009 In addition, we report for the first time a pronounced
1010 anomaly in the n-n angular distributions from photofis-
1011 sion, in which the rate of neutron emission at opening
1012 angles near 180° is diminished, resulting in a local max-
1013 imum at about 160° instead of the expected 180° . We
1014 offer two possible explanations for this effect. First, it is
1015 possible that there is a decrease in neutron emission along
1016 the fission axis. Second, the neutrons may indeed be
1017 emitted isotropically in the rest frame of each fission frag-
1018 ment, but there is a decrease in neutron emission along
1019 the fission axis because one fragment essentially shad-
1020 ows the neutrons emitted from the other fragment, ei-
1021 ther through absorption or scattering. While these mea-
1022 surements do not provide a definitive interpretation of
1023 this decreased n-n correlation for large opening angles in
1024 photofission, further study has the potential to shed light
1025 on the time evolution of neutron emission in photofission.

1026 These first measurements of n-n correlations in
1027 photofission have the potential to provide the impetus
1028 for future modeling of the fundamental physics of fission.

1029

VIII. ACKNOWLEDGMENTS

1030 This work has been supported by the National Nuclear
1031 Security Administration, grant DE-NA002488. We wish
1032 to thank the staff of the Idaho Accelerator Center for
1033 their assistance in this work. We also wish to acknowl-
1034 edge early contributions to this work by our friend and
1035 colleague the late David V. Jordan of the Pacific North-
1036 west National Laboratory.

1037 [1] S Nair, D B Gayther, B H Patrick, and E M Bowey. 1042
1038 Fission-neutron and fragment angular distributions from 1043
1039 threshold photofission of ^{232}Th and ^{238}U . *Journal of 1044*
1040 *Physics G: Nuclear Physics*, 3(7):965, 1977. URL <http://stacks.iop.org/0305-4616/3/i=7/a=010>.
1041

1042 [2] J. T. Caldwell, E. J. Dowdy, R. A. Alvarez, B. L.
1043 Berman, and P. Meyer. Experimental determina-
1044 tion of photofission neutron multiplicities for ^{235}U , ^{236}U ,
1045 ^{238}U , and ^{232}Th using monoenergetic photons. *Nu- 1046*
1047 *clear Science and Engineering*, 73(2):153–163, 1980. doi:
1048

- 1047 10.13182/NSE80-A18695. URL <https://doi.org/10.13182/NSE80-A18695>.
 1048 1098 1099
- 1049 [3] G. A. Petrov. Current status of the search for scission 1100 neutrons in fission and estimation of their main charac- 1101 teristics. *AIP Conference Proceedings*, 798(1):205–212, 1102 2005.
 1050 1103
 1051 [4] Harry R. Bowman, Stanley G. Thompson, J. C. D. Mil- 1104 ton, and Wladyslaw J. Swiatecki. Velocity and angular 1105 distributions of prompt neutrons from spontaneous fis- 1106 sion of Cf²⁵². *Phys. Rev.*, 126:2120–2136, Jun 1962. doi: 1107 10.1103/PhysRev.126.2120. URL <https://link.aps.org/doi/10.1103/PhysRev.126.2120>.
 1108 1109
 1052 [5] C. Budtz-JÃžrgensen and H.-H. Knitter. Simultane- 1110 ous investigation of fission fragments and neutrons in 1111 252Cf (SF). *Nuclear Physics A*, 490(2):307 – 328, 1988. 1112 ISSN 0375-9474. doi:[https://doi.org/10.1016/0375-9474\(88\)90508-8](https://doi.org/10.1016/0375-9474(88)90508-8). URL <http://www.sciencedirect.com/science/article/pii/0375947488905088>.
 1113 1114
 1053 [6] P. Talou, R. Vogt, J. Randrup, M. E. Rising, S. A. 1116 Pozzi, J. Verbeke, M. T. Andrews, S. D. Clarke, P. Jaf- 1117 kfe, M. Jandel, T. Kawano, M. J. Marcath, K. Meier- 1118 bachtol, L. Nakae, G. Rusev, A. Sood, I. Stetcu, and 1119 C. Walker. Correlated prompt fission data in trans- 1120 port simulations. *The European Physical Journal A*, 54 1121 (1):9, Jan 2018. doi:10.1140/epja/i2018-12455-0. URL 1122 <https://doi.org/10.1140/epja/i2018-12455-0>.
 1123
 1054 [7] S. Debenedetti, J. E. Francis, W. M. Preston, and T. W. 1124 Bonner. Angular dependence of coincidences between 1125 fission neutrons. *Phys. Rev.*, 74:1645–1650, Dec 1948. 1126 doi:10.1103/PhysRev.74.1645. URL <https://link.aps.org/doi/10.1103/PhysRev.74.1645>.
 1127
 1055 [8] J. S. Pringle and F. D. Brooks. Angular correla- 1129 tion of neutrons from spontaneous fission of ²⁵²Cf. 1130 *Phys. Rev. Lett.*, 35:1563–1566, Dec 1975. doi: 1131 10.1103/PhysRevLett.35.1563. URL <https://link.aps.org/doi/10.1103/PhysRevLett.35.1563>.
 1132 1133
 1056 [9] J. M. Verbeke, L. F. Nakae, and R. Vogt. Neutron- 1134 neutron angular correlations in spontaneous fission of 1135 ²⁵²Cf and ²⁴⁰Pu. *Phys. Rev. C*, 97:044601, Apr 2018. 1136 doi:10.1103/PhysRevC.97.044601. URL <https://link.aps.org/doi/10.1103/PhysRevC.97.044601>.
 1137 1138
 1057 [10] Sara A. Pozzi, Brian Wieger, Andreas Enqvist, Shaun D. 1139 Clarke, Marek Flaska, Matthew Marcath, Edward 1140 Larsen, Robert C. Haight, and Enrico Padovani. Corre- 1141 lated neutron emissions from ²⁵²Cf. *Nuclear Science and 1142 Engineering*, 178(2):250–260, 2014. doi:10.13182/NSE13- 1143 96. URL <https://doi.org/10.13182/NSE13-96>.
 1144 1145
 1058 [11] A. M. Gagarski, I. S. Guseva, V. E. Sokolov, G. V. 1145 Val'ski, G. A. Petrov, D. O. Krinitzin, D. V. Nikolaev, 1146 T. A. Zavarukhina, and V. I. Petrova. Neutron-neutron 1147 angular correlations in spontaneous fission of ²⁵²Cf. *Bul- 1148 letin of the Russian Academy of Sciences, Physics*, 72: 1149 773–777, July 2008. doi:10.3103/S1062873808060130.
 1150
 1059 [12] V. E. Sokolov and G. A. Petrov. Investigation of the an- 1151 gular dependences of neutron-neutron coincidences from 1152 252Cf, 235U, 233U and 239Pu fission in search of scission 1153 neutrons. *Proc. XVIII Internat. Seminar on Interaction 1154 of Neutrons with Nuclei (ISSIN-18)*, pages 108–118, 2010.
 1155
 1060 [13] Matthew J. Marcath, Tony H. Shin, Shaun D. Clarke, 1156 Paolo Peerani, and Sara A. Pozzi. Neutron angular dis- 1157 tribution in plutonium-240 spontaneous fission. *Nuclear 1158 Instruments and Methods in Physics Research, Section 1159 A: Accelerators, Spectrometers, Detectors and Associated 1160 Equipment*, 830:163–169, 9 2016. ISSN 0168-9002. doi: 1161 10.1016/j.nima.2016.05.064.
 1162
 1061 [14] Jefferson Lab. *CODA 2.6*, 2015. URL <https://coda.jlab.org/drupal>.
 1163
 1062 [15] Sara A. Pozzi, Enrico Padovani, and Marzio Marseguerra. 1164 MCNP-PoliMi: a Monte-Carlo code for correlation 1165 measurements. *Nuclear Instruments and Methods in Physics 1166 Research Section A: Accelerators, Spectrometers, Detectors 1167 and Associated Equipment*, 513(3):550 – 558, 2003. ISSN 0168-9002. doi: 1168 <https://doi.org/10.1016/j.nima.2003.06.012>. URL 1169 <http://www.sciencedirect.com/science/article/pii/S0168900203023027>.
 1170
 1063 [16] Eric C. Miller, Shaun D. Clarke, Marek Flaska, Sara 1171 A. Pozzi, and Enrico Padovani. MCNPX-PoliMi post- 1172 processing algorithm for detector response simulations. 1173 *JNMM, Journal of the Institute of Nuclear Materials 1174 Management*, 40(2):34–41, 12 2012. ISSN 0893-6188.
 1175
 1064 [17] Lawrence Berkeley National LaboratoryLawrence Liver- 1176 more National LaboratoryLos Almost National LaboratoryUniversity of Michigan Nuclear Engineering. 1177 *FREYA 2.0.3*, 2016. URL <https://nuclear.llnl.gov/simulation/main.html>.
 1178
 1065 [18] S. D. Clarke, B. M. Wieger, A. Enqvist, R. Vogt, 1179 J. Randrup, R. C. Haight, H. Y. Lee, B. A. Perdue, 1180 E. Kwan, C. Y. Wu, R. A. Henderson, and 1181 S. A. Pozzi. Measurement of the energy and multi- 1182 plicity distributions of neutrons from the photofission 1183 of ²³⁵U. *Phys. Rev. C*, 95:064612, Jun 2017. doi: 1184 10.1103/PhysRevC.95.064612. URL <https://link.aps.org/doi/10.1103/PhysRevC.95.064612>.
 1185
 1066 [19] Krishichayan, M. Bhike, A. P. Tonchev, and W. Tornow. 1186 Fission product yield measurements using monoenergetic 1187 photon beams. In *European Physical Journal Web of 1188 Conferences*, volume 146 of *European Physical Journal 1189 Web of Conferences*, page 04018, September 2017. doi: 1190 10.1051/epjconf/201714604018.
 1191
 1067 [20] Kyle Crammer. Kernel estimation in high-energy 1192 physics. *Computer Physics Communications*, 136(3): 1193 198–207, 2001.
 1194 1195
 1068 1196
 1069 1197